Hyperspectral structured LSFM for accurate and quantitative imaging

Sébastien Crombez, Cédric Ray, Chloé Exbrayat-Heritier, Florence Ruggiero, Nicolas Ducros

Hyperspectral structured LSFM for accurate and quantitative imaging

Sébastien Crombez[1,2], Cédric Ray[1,2], Chloé Exbrayat-Héritier[3], Florence Ruggiero[3], Nicolas Ducros[1,4*]

[1]INSA-Lyon, Université Claude Bernard Lyon 1, CNRS, Inserm, CREATIS UMR 5220, U1294, F-69621, LYON, France.
[2]Université Claude Bernard Lyon 1, CNRS, Institut Lumière Matière, F-69622, Villeurbanne, France.
[3]Institut de Génomique Fonctionnelle de Lyon, ENS-Lyon, UMR CNRS 5242, Universite Claude Bernard Lyon 1, Lyon Cedex, France.
[4]Institut Universitaire de France, France.

*Corresponding author(s). E-mail(s): nicolas.ducros@creatis.insa-lyon.fr;

Abstract

Light sheet fluorescence microscopy (LSFM) is a widely used technique for imaging cleared tissues and living samples. However, like most filter-based fluorescence techniques, LSFM cannot quantitatively image samples with autofluorescence or multiple fluorophores with overlapping spectra. In this study, we introduce hyperspectral structured LSFM that combines structured illumination in one spatial dimension with a data-driven algorithm based on a neural network and a physical model of the acquisition process. Our hyperspectral structured LSFM approach enables the robust reconstruction of hyperspectral data in samples with multiple fluorophores, in addition to the quantitative estimation of the abundance of each fluorophore present. We demonstrate the efficiency of our hyperspectral structured LSFM approach by imaging zebrafish embryos in 3D, illustrating autofluorescence removal and the separation of two spectrally overlapping red fluorophores. Hyperspectral structured LSFM paves the way for versatile high-resolution, quantitative hyperspectral imaging in biomedical research.

Keywords: Fluorescence microscopy, hyperspectral imaging, quantitative imaging, computational imaging, structured illumination, image reconstruction, spectral unmixing, deep learning. [Compiled on December 6, 2024]

1 Introduction

Light sheet fluorescence microscopy (LSFM) enables 3D images of fluorescent samples to be captured with low photobleaching, high acquisition speeds and high depth penetration [1]. The ability to acquire images of live specimens over extended periods [2] has made LSFM the tool of choice in developmental biology and cell biology [3]. In short, LSFM involves the illumination of a thin plane of the sample, which matches the focal plane of the detection optics [4, 5]. A myriad of design variants have emerged, facilitating the study of organ morphogenesis and function across diverse specimens including cellular spheroids, Drosophila embryos, zebrafish embryos, larvae and other model organisms [4, 6].

Similar to most fluorescence imaging techniques, LSFM requires that optical filters are chosen to retain the fluorescence emitted by fluorophores of interest while rejecting all other undesired light. In studies involving the quantification of fluorescent markers or proteins expressed in transgenic models, the presence of autofluorescence is highly detrimental as it compromises any quantitative assessment. Moreover, the analysis of samples with multiple fluorophores is strongly limited, if not impossible, with filter-based systems. In particular, spectrally-overlapping fluorophores cannot be resolved [7].

Hyperspectral imaging - whereby the light spectrum is measured in hundreds of channels over several hundred nanometres - has enabled to overcome both issues in fields such as remote sensing and medical imaging [8]. Hyperspectral LSFM was introduced by Jahr et al. [9] with a system that scans an illumination line. Although effective, the approach requires complex synchronisation between illumination, detection and fast cameras. Alternatively, image mapping spectrometry enables snapshot imaging [10], though the spatial and/or spectral resolution is compromised by the remapping strategy. Rocha-Mendoza et al. [11] have demonstrated Raman LSFM with high-speed, electronically-controlled tunable filters without moving parts, but light collection is poor [12]. The speed of Raman LSFM was later improved by Müller et al. [13] using a Fourier-transform imaging spectrometer [14] that involves the acquisition of multiple images at varying optical path differences between

the two arms of the spectrometer. More recently, LSFM has successfully adopted the concept of phasor-based hyperspectral snapshot imaging [14–16]. Though the technique only requires a pair of filters with sine/cosine transmission spectra, thereby conferring high speed and sensitivity, it assumes that only a few parameters are required to describe the measured spectra [17].

While the first generations of hyperspectral imagers were hardware-driven, more recent versions are computational systems that reconstruct the hypercube from raw measurements using dedicated algorithms [18]. This trend has been driven by the breakthrough of compressed sensing theory [19], that provides a theoretical framework for the perfect recovery of signals from few measurements. Deep learning, after revolutionising the field of computer vision [20], has also emerged as a powerful tool for image reconstruction [21], in particular in computational optics problems [22] including multispectral imaging [23, 24]. Compared to the sparsity-promoting algorithms used in compressed sensing theory, data-driven algorithms based on deep learning not only improve image quality but also accelerate the reconstruction time [22].

In this study, we present a computational strategy for LSFM, which enables imaging at high spectral resolution thanks to structured illumination. Our hyperspectral structured LSFM approach is inspired by single-pixel imaging [25–28] and illustrated in Figure 1. The fluorescence signal emitted by the light sheet is focused onto the entrance slit of an imaging spectrometer. Spatially-encoded light sheets are achieved using a digital micromirror device (DMD) in order to recover the spatial dimension orthogonal to the slit that is lost during the acquisition process. Inspired by algorithms designed for single-pixel imaging (e.g., see [29]), we introduce a data-driven reconstruction algorithm capable of recovering the lateral dimension from the modulated measurements. Our algorithm also incorporates the physical model of the structured light sheets, while benefiting from recent advances in deep learning. Finally, a spectral unmixing algorithm is integrated into our pipeline to

separate and quantify the spectral components of the sample. Our hyperspectral structured LSFM approach supports both conventional and hyperspectral LSFM, in addition to quantitative imaging in samples with multiple fluorophores. We demonstrate the capability of hyperspectral structured LSFM in terms of autofluorescence removal in zebrafish samples, in addition to the spectral separation of DsRed and mRFP, two red fluorescent proteins with overlapping emission spectra. Hyperspectral structured LSFM opens the door to high-resolution, quantitative hyperspectral imaging in biomedical research.

2 Results

2.1 Structured light sheet

Conventional LSFM illuminates the sample from the side with a uniform sheet of light [30]. In contrast, our hyperspectral approach is based on structured sheets that are modulated along the dimension orthogonal to the propagation axis (see Fig. 1b). We achieve the structured sheets by illuminating a DMD with a Gaussian beam. We then focus the light using a lens (see L in Fig. 1b) and an illumination objective (see O1 in Fig. 1b). A diaphragm must be placed at the focal point of the lens (see D Fig. 1b) to filter out the diffraction pattern created by the DMD. The generation of the structured light sheet is computer-controlled by uploading appropriate spatial patterns onto the DMD (see Fig. 1c). The optical layout of our hyperspectral structured LSFM device is provided in Section 1 of Supplementary material.

The transverse modulation of the sheet is controlled by the transverse modulation of the DMD pattern, while its thickness is controlled by the height of the DMD pattern. Great care must be taken to cope with diffraction. We retain only the zero-th diffraction order to maximise the illumination uniformity along the optical axis (see Section 2 of Supplementary material). While previous attempts to combine a cylindrical lens with a DMD resulted in a bulky system with low spatial frequency modulation [31], our DMD-only approach is compact and demonstrates improved spatial resolution. Our system produces

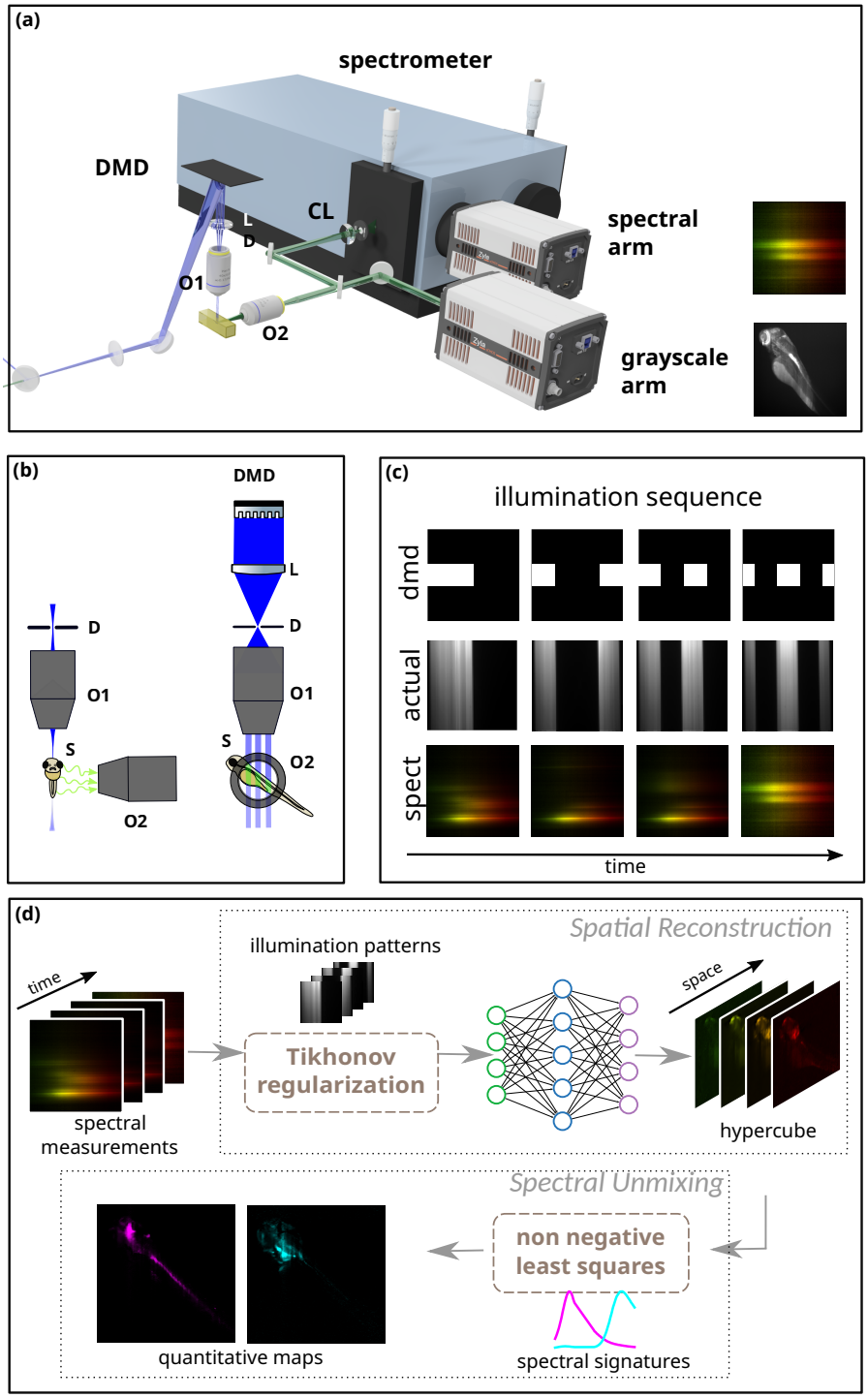

Fig. 1: Overview of hyperspectral structured LSFM. **a**, Fluorescence from the illuminated sheet is focused onto the entrance slit of an imaging spectrometer (spectral arm); the same signal can also be imaged directly by camera (grayscale arm). **b**, To recover the spatial dimension orthogonal to the slit, which is lost during acquisition, the illumination sheet is modulated transversally using a DMD. D: diaphragm; DMD: digital micromirror device; L: lens; O1 and O2: objectives; S: sample. **c**, A sequence of measurements is acquired by the spectral arm by uploading several modulation patterns onto the DMD. **d**, The hypercube is recovered from the sequence of spectral measurements by a data-driven reconstruction algorithm that combines knowledge of the actual illumination patterns, Tikhonov regularisation and a convolutional neural network. Given the spectral signature of the components of the specimen, a non-negative least squares unmixing algorithm then quantifies the concentration of the fluorescent proteins of interest.

sharp optical sectioning, generating 1.5×1.5 mm^2 structured sheets whose thickness can be computer-controlled down to 8 µm (FWHM, see Section 3 of Supplementary material). Using 128 modulation patterns, sharp transverse modulations are produced that translate into a transverse resolution of 16 µm for a longitudinal resolution of 7 µm (see Section 4 of Supplementary material).

Hadamard modulation profiles were chosen to benefit from Fellgett's advantage, gained from the acquisition of multiplexed rather than direct measurements [32]. Fellgett's advantage is demonstrated by comparing the images obtained with our setup using Hadamard illuminations and line illuminations. Over the range 500–600 nm, we observe an improvement in the peak signal-to-noise ratio of 7-8 dB (see Section 7 of Supplementary material).

2.2 Double arm set-up

The fluorescence emitted within the light sheet passes through the collection objective and is sent to either a grayscale or spectral arm (see Fig. 1a). The grayscale arm corresponds to conventional LSFM, where a camera acquires the fluorescence distribution across the two spatial dimensions of the illumination plane. When a sample with homogeneously distributed florescence is considered, the grayscale arm acquires the distribution of light within the illumination plane, which corresponds to the actual illumination profile and differs from the profile uploaded onto the DMD (see Fig. 1c). The grayscale arm is therefore capable of both conventional LSFM and calibration of the modulation profiles of the structured light sheets. Knowledge of the actual illumination profiles is a critical aspect of the reconstruction algorithm.

In the spectral arm, a camera acquires images that represent spectra along the entrance slit of the spectrometer after integration in the transverse direction (Fig. 1c and Visualisation 1). The transverse spatial dimension can be recovered by exploiting the spectral

images acquired using several illumination profiles. We consider a Czerny-Turner spectrometer with a 300 line/mm grating leading to a spectral resolution of 2 nm across a bandwidth of 108 nm.

2.3 Two-step algorithm for reconstruction and unmixing

We recover the quantitative abundance maps of fluorophores using the two-step algorithm depicted in Figure 1d and detailed in Section 4. The first step reconstructs the transverse spatial dimension lost during acquisition, while the second step unmixes the multiple spectral components (e.g., fluorophores) of the hypercube, leading to quantitative abundance maps.

The first reconstruction step assumes knowledge of the modulation patterns acquired by the grayscale arm (see Fig. 6 of Supplementary material). By concatenating all patterns, we build the measurement matrix that models the acquisition process. As its inversion tends to amplify noise, the inverse problem is stabilised by combining Tikhonov regularisation and a convolutional neural network. While Tikhonov regularisation applies to only the transverse direction, the neural network applies across both spatial dimensions, hence regularising both the transverse and longitudinal directions. The neural network is a U-Net whose parameters are trained end-to-end, such that the reconstruction pipeline minimises the empirical mean squared error of the imageNet database (see Eq. (5) in Section 4.4).

The second spectral unmixing step recovers the quantitative abundance maps of the fluorescent proteins present in the sample by solving a non-negative least squares minimisation problem. To do so, we assume that the number of components and each of their spectra are known (see Eq. (6) in Section 4.5). In the case of transgenic animal models, the expressed florescent proteins are well known and characterised. The autofluorescence spectrum needs to be estimated in situ, achieved by considering pixels in anatomical regions (e.g., yolk sac) where autofluorescence accumulates and no specific fluorescence of interest is expressed

2.4 Autofluorescence removal

We demonstrate quantitative imaging with autofluorescence removal in a 4-day-old Tg(fli1:EGFP;olig2:DsRed) zebrafish larva (Fig. 2). This fluorescent transgenic reporter line specifically expresses the fluorescent proteins EGFP (Enhanced Green Fluorescent Protein) and DsRed (Discosoma sp Red fluorescent protein) under the control of fli and olig2 promoters, respectively. The EGFP and DsRed emission peaks are well separated ($\Delta\lambda_{\mathrm{em}} \approx 80$ nm, see Fig. 2j) but suffer from autofluorescence. Figure 2a presents the conventional LSFM image acquired using the grayscale arm, while Figure 2i,k present colour images acquired using a commercial confocal microscope (Zeiss LSM780) using two excitation wavelengths ($\lambda^{\mathrm{ex}}_{\mathrm{EGFP}} = 488$ nm and $\lambda^{\mathrm{ex}}_{\mathrm{DsRed}} = 561$ nm) and appropriate filters.

Figure 2g–h show the EGFP and DsRed images obtained by conventional LSFM, filtered using two virtual band-pass filters whose spectral responses (Fig. 2j) were chosen to optimise the separation of the two fluorophores while minimising autofluorescence. Fluorescence is notably observed in the yolk sac of both images (Fig. 2g–h), a region where neither fli1 nor olig2 are expressed (fli1 is expressed in the vascular system [33], olig2 in the central nervous system [34]), which thus clearly indicates that filtering does not enable the removal of autofluorescence.

Figure 2d-f show the quantitative abundance maps for EGFP, DsRed and autofluorescence obtained by hyperspectral structured LSFM. The spectral signature of EGFP and DsRed used for spectral unmixing have been taken from the Fluorescent Protein Database [35], while autofluorescence spectrum has been obtained from the yolk sac (Figure 2a). Before unmixing, the notch filter is applied to the emission spectrum of EGFP and DsRed (see Fig. 2j). The EGFP abundance map (Fig. 2d) shows the endothelial cells that are present in the entire vasculature, in particular in the intersegmental vessels in the trunk and head, while the DsRed abundance map (Fig. 2e) shows the neural progenitors and oligodendrocytes that are present in the brain, retina and spinal cord, confirming the effectiveness of our approach. Furthermore, the autofluorescence abundance map (Fig. 2f)

reveals that distribution is not uniform and consequently, that autofluorescence correction based on the conventional LSFM filter-based approach is inaccurate.

Figure 2b-c show the sample in, respectively, 2D and 3D after autofluorescence removal, obtained from the EGFP and DsRed quantitative abundance maps. The 3D images (Fig. 2c) represents 25 adjacent slices resulting in $512 \times 512 \times 25$ voxels of size $3 \times 3 \times 15$ μm^3, enhancing the structural and molecular understanding of the sample. The quantitative abundance maps and conventional LFSM images of the different slices are displayed in Fig. 8 and Fig. 9 of Supplementary material, respectively (see also Visualisation 2 and Visualisation 3).

2.5 Separation of overlapping fluorophores

We demonstrate the spectral separation of two red fluorescent proteins in a 4-day-old Tg(sox10:mRFP;olig2:DsRed) zebrafish larva (see Fig. 3). Olig2 is expressed in the central nervous system, in particular the spinal cord [34], while sox10 is expressed in the neural cell and in the neural crest-derived Schwann cells located in the peripheral nervous system [36]. Separating sox10 from olig2 is particularly challenging due to the spectral overlap of the emission spectra of mRFP (monomeric Red Fluorescent Protein) and DsRed ($\Delta\lambda_{\mathrm{em}} \approx 20$ nm, see Fig. 3j), as well as the spatial overlap of the sox10 and olig2 signal in the head and neural tube.

Figure 3a presents the conventional LSFM image acquired with the grayscale arm, while Figure 3b–c present quantitative abundance maps of mRPF and DsRed (one slice of the sample in b, 3D representation in c) obtained by hyperspectral structured LSFM. Figure 3i,k show the images obtained using a confocal microscope (Zeiss LSM780, $\lambda^{\mathrm{ex}} = 561$ nm). Figure 3g–h show the images obtained by filtering conventional LSFM with two band-pass filters whose spectral responses were chosen to optimise the separation of mRFP and DsRed (see Fig. 3j). Despite these efforts, the mRFP and DsRed filtered images (Fig. 3g–h) are highly correlated, indicating significant overlap between the two

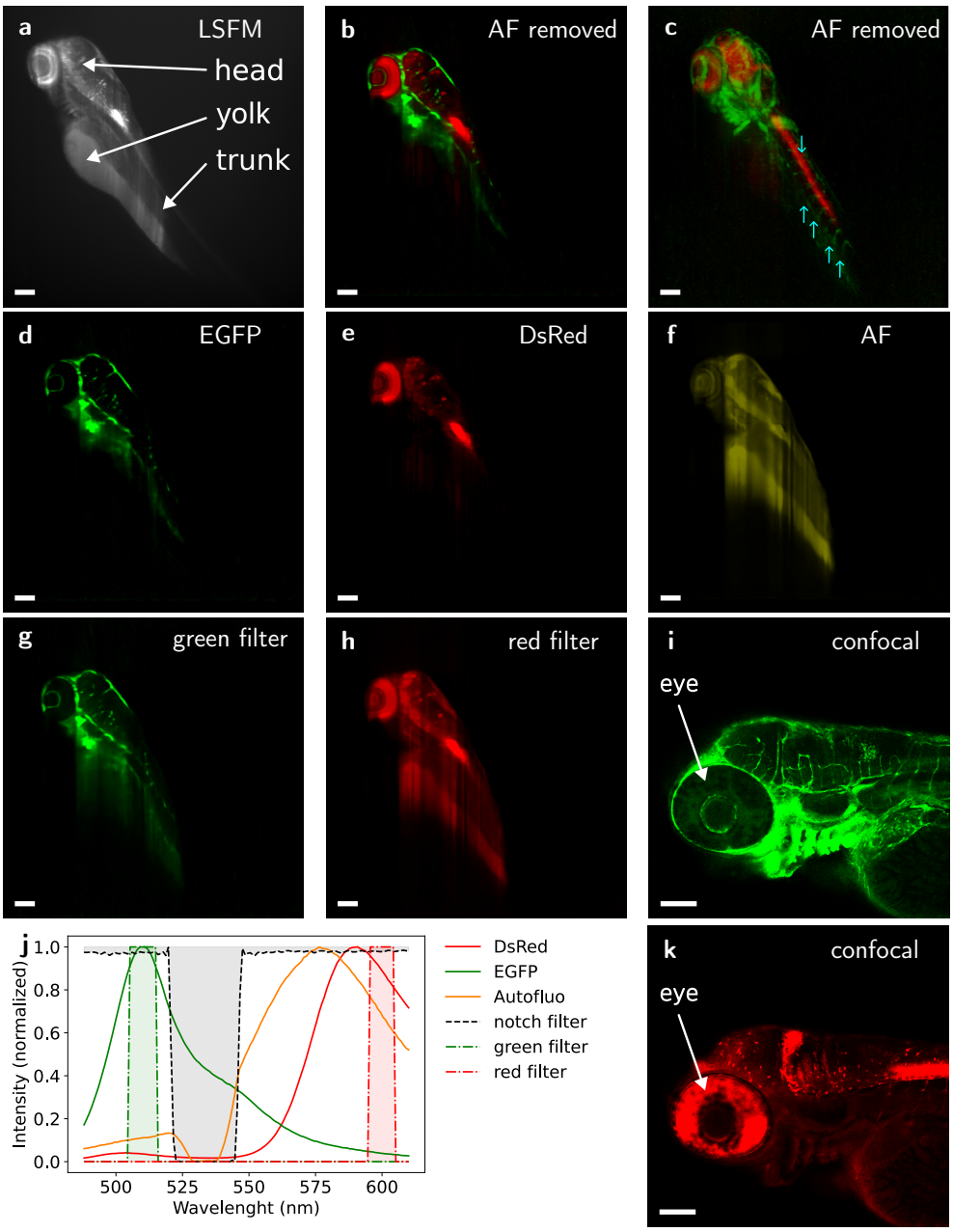

Fig. 2: Autofluorescence removal in a 4-day-old Tg(fli1:EGFP;olig2:DsRed) zebrafish larva. **a**, Conventional LSFM image acquired using the grayscale arm. **b–f**, Quantitative abundance maps obtained from hyperspectral structured LSFM. **b–c**, Images after autofluorescence (AF) removal showing only the abundance of EGFP (in green) and DsRed (in red); **b** is the same slice as in **a**; **c** is the 3D representation obtained from 25 slices. (↓) points to the spinal cord, (↑) indicate the intersegmental vessels. **d–f**, Quantitative abundance maps of EGFP, DsRed and autofluorescence (AF) obtained using the spectra in **j** for unmixing; Superposing **d** and **e** leads to **b**. **g–h**, Images of EGFP and DsRed obtained by conventional LSFM, filtered using the two band-pass filters in **j**. **i,k**, Head of the embryo imaged by a commercial confocal microscope (Zeiss LSM780 using optical filters ([ref]). **j**, Filters (dashed lines) and fluorescence spectra for spectral unmixing (solid lines). Lateral views, anterior is left. Scale bars = 100 µm.

fluorophores. More specifically, the mRFP image exhibits high intensity in the spinal cord, confirming that the filtering strategy fails to separate mRFP from DsRed. Figure 3d–f show the mRFP, DsRed and autofluorescence quantitative abundance maps obtained by hyperspectral structured LSFM. The spectral signatures of mRFP and DsRed used for unmixing have been taken from the Fluorescent Protein Database [35], while that of autofluorescence has been measured in the yolk sac (see spectra in Fig. 3j).

By exploiting the full spectrum, the hyperspectral structured LSFM pipeline successfully separates mRFP from DsRed despite their overlapping spectra. In the quantitative abundance maps, the mRFP signal is only observed in the neural crest cells in the brain (see Fig. 3d), while DsRed concentrates in the brain, retina and spinal cord (see Fig. 3e), confirming the effectiveness of our approach. Considering the cerebellum, in which olig2 is specifically expressed, this structure can be observed in both the mRFP and DsRed images obtained by filtered conventional LSFM (Fig. 3.g-h). Conversely, the cerebellum is visible only in the DsRed and not mRFP quantitative abundance maps acquired using the hyperspectral structured LSFM pipeline (Fig. 3.d-e). Similarly to the previous example, the autofluorescence abundance map is found to vary spatially (see Fig. 3f), indicating that the conventional LSFM filter-based approach is inaccurate. It should be noted, however, that the concentration of autofluorescence around the spinal cord (see Fig. 3f) may be due to unmixing inaccuracies.

Figure 3c shows the distribution of DsRed and mRFP in 3D, obtained from the quantitative abundance maps of 20 adjacent slices resulting in $512 \times 512 \times 20$ voxels of size $3 \times 3 \times 15$ μm^3. The quantitative abundance maps of all slices are displayed in Fig. 10 of Supplementary material (see also Visualisation 4).

3 Discussion

We have demonstrated hyperspectral LSFM by shaping structured light sheets using only a DMD. Our optical system is simple, with no moving parts, few optical elements and does

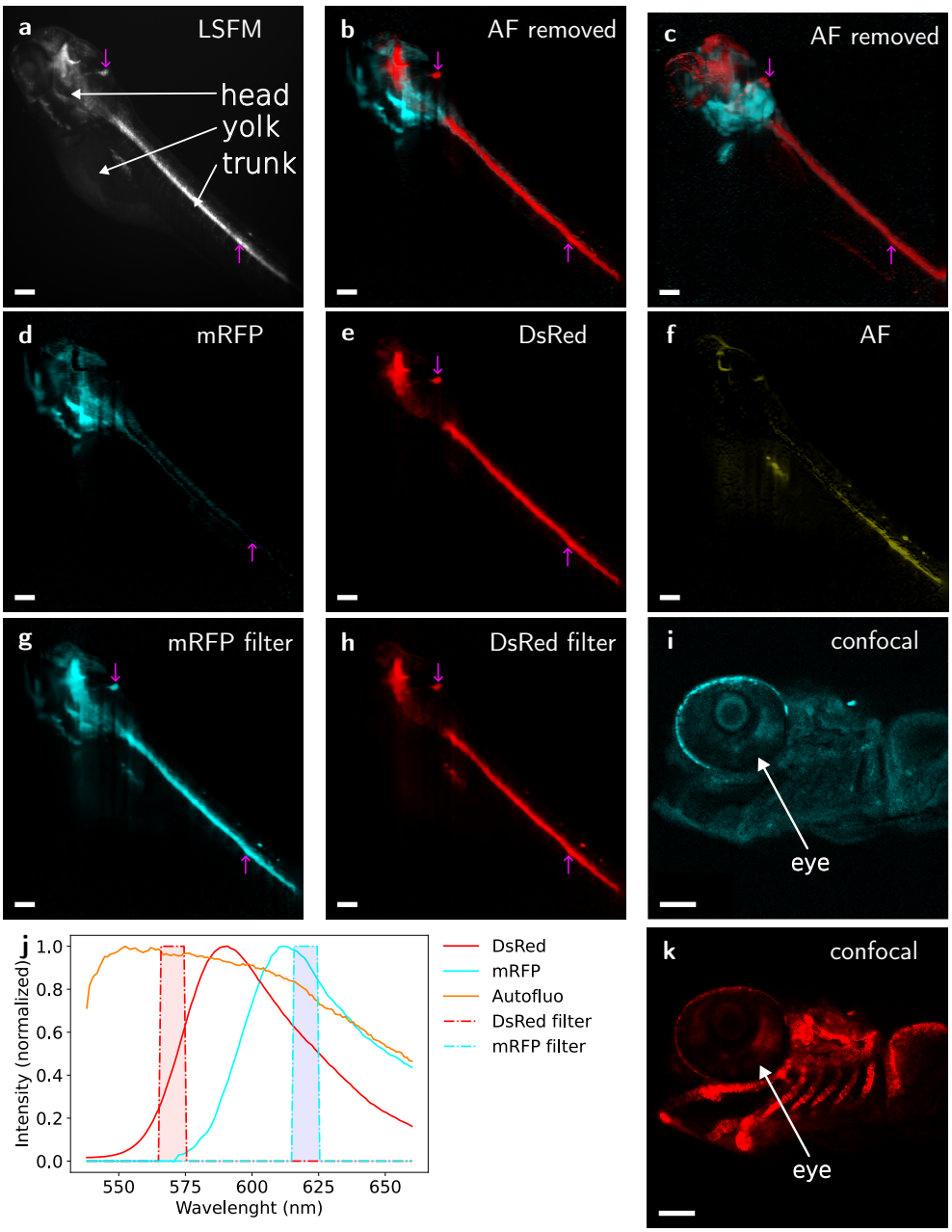

Fig. 3: Separation of fluorescent proteins with overlapping spectra. The sample is a 4-day-old Tg(sox10:mRFP;olig2:DsRed) zebrafish larva. **a–h**, Entire embryo imaged using conventional and hyperspectral structured LSFM. **a**, Conventional LSFM image acquired using the grayscale arm. **b–c**, Quantitative abundance maps after autofluorescence (AF) removal obtained using hyperspectral structured LSFM; **b** is the same slice as in **a**; **c** is the 3D representation obtained from 20 slices. **d–f**, Quantitative abundance maps of mRFP, DsRed and autofluorescence obtained by hyperspectral structured LSFM using the spectra in **j** for unmixing. **g–h**, Images obtained by filtering conventional LSFM using the two band-pass filters whose response are depicted in **j**. **i,k**, Head of the embryo imaged by a commercial confocal microscope (Zeiss LSM780 using optical filters ([ref]). **j**, Filters (dashed lines) and fluorescence spectra for spectral unmixing (solid lines).(↑) point to the spinal cord, (↓) indicate the cerebellum. Lateral views, anterior is left. Scale bars = 100 µm.

not require fast cameras. It can be combined with any standard filter-based light sheet microscopes. While LSFM is dominated by grayscale imaging, the palette of genetically encoded and synthesized fluorophores has enabled the labelling and observation of a large and constantly expanding number of molecular species [37]. Hyperspectral imaging offers the possibility of studying multiple components, cellular behaviours and cellular metabolism within the same specimen. In [9], the authors achieved hyperspectral imaging based on pushbroom acquisitions. Illuminating only a line of the imaging plane at a time, however, reduces light throughput compared to hyperspectral structured LSFM which illuminates approximately half of the imaging plane at a time. The higher throughput of hyperspectral structured LSFM translates into the so-called Fellgett's advantage [38], an improved signal-to-noise ratio that we have quantified as 7–8 dB in our configuration (see Sec. 6 of Supplementary material).

Hyperspectral alternatives based on tunable filers reject a large fraction of the fluorescent signal emitted by the sample [12], leading to poor light collection and increased photobleaching compared to hyperspectral structured LSFM that exploits all emitted fluorescence photons. The snapshot imager introduced in [10] is fast but imposes a tradeoff between the field of view and the spectral resolution, whereas hyperspectral structured LSFM, though slower due to is sequential nature, offers higher spectral resolution (e.g., <4 µm) over a larger field of view (e.g., 1.5×1.5 mm^2). The spectral resolution is determined by the focal length of the cylindrical lens, the slit width and the grating of the spectrometer. Raw acquisitions include 2,048 spectral channels that we have binned to 128 channels to match the spectral resolution of the spectrometer (2 nm, see Sec. 4 of Supplementary material) achieved with a 600 µm slit. We have chosen the largest slit available in order to maximise light throughput while ensuring the different fluorophores can be resolved.

While the longitudinal resolution along the slit of the spectrometer depends only on the collection objective, the transverse resolution transverse to the slit of the spectrometer is limited by the number of patterns displayed on the DMD and our ability to engineer systems

capable of generating high-frequency structured light sheets. Using a collection objective with a low numerical aperture (NA $= 0.1$, at 500 nm theoretical Rayleigh resolution of $\sim$3 µm and focal depth of $\sim$50 µm), we have achieved a lateral resolution of 7 µm for a longitudinal resolution of 15 µm using 128 patterns (see Sec. 4 of Supplementary material) over a field of view of 1.5 mm^2. Higher spatial resolutions could be achieved using collection objectives with higher numerical aperture. Moreover, it has been shown that structured illumination LSFM can achieve resolutions below 100 nm in the lateral direction [39], while random illuminations can also break the diffraction limit [40]. The spatial resolution of hyperspectral structured LSFM is therefore ultimately limited by the number of patterns and light throughput, leading to a trade-off between the spatial resolution and the imaging speed in the longitudinal dimension. The spatial resolution could also be improved using software that incorporates the conventional LSFM images acquired using the grayscale arm, a technique known as pansharpening in remote sensing [41]. By shaping the light using a DMD, we can numerically adjust both the thickness of the light sheets and the transverse resolution, providing a high degree of flexibility to adapt to different samples.

Considering a power of 0.64 mW at the sample plane, hyperspectral structured LSFM acquired more that $65,000 \times 128$ pixels (spatial $\times$ spectral) in approximately 5 min 30 s (see Table 3 of Supplementary material). The method in [9] achieved shorter acquisition times (down to 1.5 s) but with higher laser power (2–10 mW in the back focal plane of the illumination objective) and for only $2,000 \times 70$ pixels (spatial $\times$ spectral). For fair comparison, we introduce the power-time budget per pixel (see Section 5 of Supplementary material). The lower the power-time budget per pixel, the faster. While the pushbroom method in [9] works at $\sim$200 µW.ms/pixel, hyperspectral structured LSFM requires only 40–50 µW.ms/pixel (2–3 µW.ms/pixel before binning raw measurements), which constitutes an acceleration of one or two orders of magnitude. The acquisition of multiple slices has been done sequentially by translating the sample. The acquisition of multiple slices using hyperspectral structured LSFM could be further accelerated by exploiting structured

light sheets in the translation direction, in a similar fashion to [42, 43], or even adapting the modulation to the sample, in line with the smart microscopy trend [44].

We have proposed a fast, simple yet effective, data-driven reconstruction method. Building on [29], our algorithm has only two steps. Alternatives include iterative algorithms based on the concept of unrolling [45] or plug-and-play [46] methods. The different spectral channels of the same hypercube have different intensities and hence different noise levels. It is therefore key to adapt regularisation to the noise level. In this regard, the Tikhonov step was found to generalise better to unseen noise levels than simpler alternatives based on the computation of the pseudo inverse solution, in accordance with previous studies [29]. Our approach reconstructs all spectral channels independently. More demanding alternatives could consider reconstruction strategies working across both the spatial and spectral dimensions, i.e., handling the different spectral channels jointly (e.g., see [47]). Here again, great care should be taken to avoid spectral distortions that would significantly degrade our ability to unmix the spectral components in the sample. The approach developed in [15] is fit-free and does not require any prior assumptions about the components. However, it assumes that a only few parameters are required to describe the measured spectra. Here, we have assumed that the emission spectra of the fluorescent proteins are known and constant across the sample, hence discarding spectral changes due to the local environment. However, the assumption may not be met in other samples. In this case, the spectra can be estimated together with the quantitative abundance maps. This problem, referred to as non-negative matrix factorisation, has a long history in statistics and linear algebra [48] but is much harder to solve.

4 Method

4.1 Transgenic lines and sample preparation

The transgenic fluorescent zebrafish lines: Tg(fli1:EGFP), Tg(olig2:DsRed) and Tg(sox10:mRFP), were produced at the zebrafish PRECI facility (Plateau de Recherche

Expérimentale de Criblage In vivo, SFR Biosciences UAR3444/CNRS, US8/Inserm, ENS de Lyon, UCBL) in compliance with French government guidelines (agreement number C693870602). To obtain the double transgenic lines used in this study, the Tg(olig2:DsRed) fish were outcrossed with Tg(fli1:EGFP);Casper or Tg(sox10:mRFP) fish. The resulting Tg(fli1:EGFP);Casper;Tg(olig2:DsRed) and Tg(sox10:mRFP);Tg(olig2:DsRed) transgenic embryos were collected and raised under standard conditions according to the European Directive 2010/63/EU. Developmental stages are given in days post-fertilization (dpf) at 28.5°C, based on morphological criteria as previously described [2]. At 1 dpf, the embryos were treated with 0.2 mM 1-phenyl 2-thiourea (Sigma-Aldrich, France) to inhibit pigmentation. Larvae were selected based on the expression of the fluorescent proteins of interest. They were sacrificed by an overdose of anaesthetic (0.2 % Tricaine, pH 7.0) and fixed at 4-5 dpf in paraformaldehyde for 2h at room temperature. After fixation, they were washed in PBDTT (1X PBS, 1% DMSO, 0.1% Tween, 0.5% Triton; all reagents from Sigma-Aldrich, France). The samples were then placed in spectrophotometer quartz cells and embedded in 1% low melting agarose (ThermoFisher Scientific, France), or mounted on a coverslip in DAKO mouting medium using a spacer for confocal acquisition. The samples were immediately used for observation or stored at 4-5°C in the dark before observation. Confocal images were acquired with an LSM 780 and LSM 800 microscope (Zeiss, Germany). The confocal images were formatted using the 'Z projection' tool in the Fiji software for confocal images.

4.2 Acquisition model

The measurements in hyperspectral structured LSFM acquisitions originate from both the spatial mixing induced by the imaging device (see Eq. (1)) and the spectral mixing inherent to the sample (see Eq. (2) models). The measurements are modelled as

$$\boldsymbol{M}_\lambda = \boldsymbol{H}\boldsymbol{F}_\lambda + \boldsymbol{E} \quad , 1 \leq \lambda \leq \Lambda, \tag{1}$$

where $\boldsymbol{H} \in \mathbb{R}^{K \times N_x}$ represents the measurement matrix that concatenates the K spatial light profiles used for acquisition, $\boldsymbol{F}_\lambda \in \mathbb{R}^{N_x \times N_y}$ is a λ-slice of the full hypercube, and $\boldsymbol{E} \in \mathbb{R}^{K \times N_y}$ represents the measurement errors. The spatial light profiles of our device are determined experimentally (see Fig. 1c; details provided in Section 3 of Supplementary material). We denote by $\boldsymbol{F} = [\mathrm{vec}\,(F_1), \ldots, \mathrm{vec}\,(F_\Lambda)]^\top \in \mathbb{R}^{\Lambda \times N}$, $N = N_x N_y$, the full hypercube arranged in matrix form by concatenating all λ-slices, representing the total number of pixels.

Assuming that the sample is made of Q distinct spectral components, the full hypercube can be modelled as

$$\boldsymbol{F} = \boldsymbol{S}\boldsymbol{A}, \tag{2}$$

where $\boldsymbol{S} \in \mathbb{R}^{\Lambda \times Q}$ represents the spectral signatures of the components, and $\boldsymbol{A} \in \mathbb{R}^{Q \times N}$ represents the quantitative abundance of each spectral component per pixel. In the case of fluorescent imaging, a component can represent either a single specific fluorophore (e.g., EGFP, DsRed or mRFP) or a combination of fluorophores (e.g., autofluorescence).

4.3 Image-domain approach

Our goal is to recover the quantitative abundance maps $\boldsymbol{A}$ from the measurements $\boldsymbol{M}_\lambda$, $1 \leq \lambda \leq \Lambda$, knowing the measurement matrix $\boldsymbol{H}$ and assuming prior knowledge about the spectral signatures $\boldsymbol{S}$. To do so, we adopt an image-domain approach that involves spatial reconstruction followed by spectral unmixing that has been found in single-pixel imaging to be more efficient and suitable than spectral unmixing before spatial reconstruction [49].

We first recover the full hypercube $\boldsymbol{F}$ (spatial reconstruction) before recovering the quantitative abundance maps $\boldsymbol{A}$ (spectral unmixing), as described below and illustrated in Figure 1.

- (Step 1: spatial reconstruction) Recover the λ-slice $\boldsymbol{F}_\lambda$ from the measurement $\boldsymbol{M}_\lambda$, for all spectral channels $1 \leq \lambda \leq \Lambda$, given the measurement matrix $\boldsymbol{H}$. This corresponds to the inversion of Eq. (1).

- (Step 2: spectral unmixing) Recover the quantitative abundance maps $\boldsymbol{A}$ from the full hypercube $\boldsymbol{F}$ calculted in step 1, given the spectral signatures $\boldsymbol{S}$. This corresponds to the inversion of Eq. (2).

4.4 Spatial reconstruction: Tikhonov-Net

We reconstruct the λ-slices using the Tikhonov-Net, a two-step reconstruction network of the form

$$\mathcal{R}_\theta = \mathcal{G}_\theta \circ \mathcal{R}, \tag{3}$$

where $\mathcal{G}_\theta : \mathbb{R}^{N_x \times N_y} \to \mathbb{R}^{N_x \times N_y}$ is a neural network with parameters θ acting in the spatial domain (e.g., a convolutional network) and $\mathcal{R} : \mathbb{R}^{K \times N_y} \to \mathbb{R}^{N_x \times N_y}$ is a mapping from the measurement domain to the spatial domain. Inspired by [29], we choose the measurement-to-spatial domain mapping $\mathcal{R}$ as Tikhonov regularisation

$$\mathcal{R}(\boldsymbol{M}_\lambda) = \boldsymbol{\Sigma}\boldsymbol{H}^\top \left(\boldsymbol{H}\boldsymbol{\Sigma}\boldsymbol{H}^\top + \boldsymbol{\Gamma}\right)^{-1} \boldsymbol{M}_\lambda, \tag{4}$$

where $\boldsymbol{\Sigma} \in \mathbb{R}^{N_x \times N_x}$ represents the slice covariance, and $\boldsymbol{\Gamma} \in \mathbb{R}^{K \times K}$ the measurement covariance. The computation of covariances $\boldsymbol{\Sigma}$ and $\boldsymbol{\Gamma}$ is described in Section 10 of Supplementary material. Note that, as stated by Eq. (4), the Tikhonov regularisation applies to the transverse x-axis only, while the neural network $\mathcal{G}$ applies to both the transverse x- and longitudinal y- axis. The image domain neural network $\mathcal{G}_\theta$, is trained end-to-end in a supervised manner, i.e.,

$$\hat{\theta} \in \operatorname*{argmin}_\theta \frac{1}{L} \sum_\ell \|\mathcal{R}_\theta(\boldsymbol{M}^\ell) - \boldsymbol{F}^\ell\|_{\mathrm{F}}^2, \tag{5}$$

where $\{\boldsymbol{F}^\ell, \boldsymbol{M}^\ell\}$, $1 \leq \ell \leq L$, is a database of L image-measurement pairs and $\|\cdot\|_{\mathrm{F}}^2$ denotes the Frobenius norm.

4.5 Spectral unmixing: non-negative least squares

We formalise spectral unmixing as the constrained least squares minimisation problem

$$\underset{\boldsymbol{A}\in\Omega}{\operatorname{argmin}} \|\hat{\boldsymbol{F}} - \boldsymbol{S}\boldsymbol{A}\|_{\mathrm{F}}^2, \tag{6}$$

where $\hat{\boldsymbol{F}} = [\hat{\mathcal{R}}(\boldsymbol{M}_1), \ldots, \hat{\mathcal{R}}(\boldsymbol{M}_\Lambda)]$ is the hypercube obtained after spatial reconstruction (see Section 4.4) and $\Omega \in \mathbb{R}^{Q\times N}$ represents the solution space. In the unconstrained case $\Omega = \mathbb{R}^{Q\times N}$, the solution is given by the pseudo inverse $\hat{\boldsymbol{A}} = (\boldsymbol{S}^\top\boldsymbol{S})^{-1}\boldsymbol{S}^\top\hat{\boldsymbol{F}}$, while the non-negative case $\Omega = \mathbb{R}_+^{Q\times N}$ requires an iterative algorithm such as [50]. Here, we assume that the spectral signatures $\boldsymbol{S}$ are known, which is the case for transgenic samples that express specific fluorescent proteins. The spectrum of autofluorescence may vary significantly across samples; however, it can be estimated from pure pixels, e.g., anatomical structures where no fluorescent proteins are present. The minimisation problem of Eq. (6) is solved using the `NNLS` function of the PySptools package.

4.6 Implementation details

We consider a sequence of $K = 128$ Hadamard patterns. We independently measure the positive components of the patterns, denoted by $\boldsymbol{H}^+$, and the negative components of the patterns, denoted by $\boldsymbol{H}^-$, where $\boldsymbol{H} = \boldsymbol{H}^+ - \boldsymbol{H}^-$ is a Hadamard matrix (see Section 3 of Supplementary material). The raw measurements $\boldsymbol{M}^+$ and $\boldsymbol{M}^-$, acquired with $\boldsymbol{H}^+$ and $\boldsymbol{H}^-$, respectively, are binned to $\Lambda = 128$ spectral channels and $N_y = 512$ pixels in the longitudinal direction. After preprocessing (see Section 9 of Supplementary material), all Λ spectral slices are reconstructed using the Tikhonov-Net given by Eq. (3), where we choose the neural network $\mathcal{G}$ as a U-Net with $499,985$ trainable parameters. The Tikhonov-Net has been integrated to SPyRiT, a python package dedicated to single-pixel imaging [51] and based on PyTorch [52]. It is trained in an end-to-end fashion from simulations considering raw data corrupted by Poisson noise with an image intensity α of 50 photons.

We consider the Adam optimiser for 20 epochs, with an initial step size of 10^{-3} that we divide by a factor of 2 every 10 epochs. We set the weight decay regularisation parameter to 10^{-7}. Our training database corresponds to the test set of the ImageNet ILSVRC2012 [53] where each of the 100k images is resized to $N_x \times N_y = 512 \times 512$. After spatial reconstruction, we compensate for a small spectral shift that is observed to vary linearly with the wavelength across the longitudinal dimension y.

Funding

Funding was received from the French National Research Agency (ANR-11-LABX-0063 and ANR-19-CE14-046) and the Institut universitaire de France (IUF).

Acknowledgements

S.C, C.R., and N.D. acknowledge support from Labex PRIMES (ANR-11-LABX-0063). N.D acknowledges support from the Institut universitaire de France (IUF) and thanks Jérémy E. Cohen for insights on linear unmixing and non-negative matrix factorisation.

Data availability

The raw measurements, preprocessed measurements, reconstructed hypercubes, filtered images and quantitative abundance maps used in this study are available in our data warehouse (currently private and accessible on demand; will be made public upon manuscript acceptance) https://pilot-warehouse.creatis.insa-lyon.fr/#collection/63caa9497bef31845d991351. This database adheres to FAIR (Findability, Accessibility, Interoperability, Reusability) principles.

Code availability

Code for generating Figure 2 and Figure 3, as well as Figure 6 and 8 of Supplementary material, can be found at https://github.com/openspyrit/spyrit-examples/tree/master-seb/2023_hsLSFM. The covariance matrix and parameters of the neural networks used for image reconstruction, as well as the spectra used for unmixing, can be found

in our data warehouse (currently private and accessible on demand; will be made public upon manuscript acceptance) https://pilot-warehouse.creatis.insa-lyon.fr/#collection/63caa9497bef31845d991351/folder/6464d57585f48d3da0718934

Ethics declarations

The authors declare no competing interests.

Supplementary material

The Supplemental Document includes a description of the experimental setup, the handling of DMD diffraction, a characterisation of the light sheet, an analysis of the resolution of the system, an analysis of the imaging speed of the system, the quantitative maps for all slices of the samples, the verification of the Fellgett's advantage, the description of the noise model of the raw data, the description of the preprocessing of the raw data, and the description of the estimation of the covariance matrices.

Visualisation 1 shows the raw measurements for one slice of the Tg(fli1:EGFP;olig2:DsRed) sample.

Visualisation 2 shows the abundance of EGFP (in green) and DsRed (in red) for all the 25 slices of the Tg(fli1:EGFP;olig2:DsRed) sample. Many more visualisations of the abundance maps can be found here.

Visualisation 3 shows the conventional LSFM images for 21 slices of the Tg(fli1:EGFP;olig2:DsRed) sample. Other conventional LSFM images of the sample can be found here.

Visualisation 4 shows the abundance of mRFP (in cyan) and DsRed (in red) for all the 20 slices of the Tg(sox10:mRFP;olig2:DsRed) sample. Many more visualisations of the abundance maps can be found here.

References

[1] Huisken, J., Stainier, D.Y.R.: Selective plane illumination microscopy techniques

in developmental biology. Development **136**(12), 1963–1975 (2009) https://doi.org/10.1242/dev.022426 . Chap. Review

[2] Stelzer, E.H.K.: Light-sheet fluorescence microscopy for quantitative biology. Nature Methods **12**(1), 23–26 (2015) https://doi.org/10.1038/nmeth.3219

[3] Weber, M., Huisken, J.: Light sheet microscopy for real-time developmental biology. Current Opinion in Genetics & Development **21**(5), 566–572 (2011) https://doi.org/10.1016/j.gde.2011.09.009

[4] Olarte, O.E., Andilla, J., Gualda, E.J., Loza-Alvarez, P.: Light-sheet microscopy: A tutorial. Advances in Optics and Photonics **10**(1), 111 (2018) https://doi.org/10.1364/AOP.10.000111

[5] Kafian, H., Mozaffari-Jovin, S., Bagheri, M., Shaegh, S.A.M.: Light-sheet fluorescent microscopy: Fundamentals, developments and applications. Physica Scripta **98**(8), 082001 (2023) https://doi.org/10.1088/1402-4896/acd7ae

[6] Wan, Y., McDole, K., Keller, P.J.: Light-Sheet Microscopy and Its Potential for Understanding Developmental Processes. Annual Review of Cell and Developmental Biology **35**(1), 655–681 (2019) https://doi.org/10.1146/annurev-cellbio-100818-125311

[7] Dickinson, M.E., Bearman, G., Tille, S., Lansford, R., Fraser, S.E.: Multi-Spectral Imaging and Linear Unmixing Add a Whole New Dimension to Laser Scanning Fluorescence Microscopy. BioTechniques **31**(6), 1272–1278 (2001) https://doi.org/10.2144/01316bt01

[8] Lu, G., Fei, B.: Medical hyperspectral imaging: A review. Journal of Biomedical Optics **19**(1), 010901 (2014) https://doi.org/10.1117/1.JBO.19.1.010901

[9] Jahr, W., Schmid, B., Schmied, C., Fahrbach, F.O., Huisken, J.: Hyperspectral light sheet microscopy. Nature Communications **6**, 7990 (2015) https://doi.org/10.1038/ncomms8990

[10] Lavagnino, Z., Dwight, J., Ustione, A., Nguyen, T.-U., Tkaczyk, T.S., Piston, D.W.: Snapshot Hyperspectral Light-Sheet Imaging of Signal Transduction in Live Pancreatic Islets. Biophysical journal **111**(2), 409–417 (2016) https://doi.org/10.1016/j.bpj.2016.06.014

[11] Rocha-Mendoza, I., Licea-Rodriguez, J., Marro, M., Olarte, O.E., Plata-Sanchez, M., Loza-Alvarez, P.: Rapid spontaneous Raman light sheet microscopy using cw-lasers and tunable filters. Biomedical Optics Express **6**(9), 3449–3461 (2015) https://doi.org/10.1364/BOE.6.003449

[12] Boldrini, B., Kessler, W., Rebner, K., Kessler, R.W.: Hyperspectral Imaging: A Review of Best Practice, Performance and Pitfalls for in-line and on-line Applications. Journal of Near Infrared Spectroscopy **20**(5), 483–508 (2012)

[13] Müller, W., Kielhorn, M., Schmitt, M., Popp, J., Heintzmann, R.: Light sheet Raman micro-spectroscopy. Optica **3**(4), 452–457 (2016) https://doi.org/10.1364/OPTICA.3.000452

[14] Morizet, J., Chow, D., Wijesinghe, P., Schartner, E., Dwapanyin, G., Dubost, N., Bruce, G.D., Anckaert, E., Dunning, K., Dholakia, K.: UVA Hyperspectral Light-Sheet Microscopy for Volumetric Metabolic Imaging: Application to Preimplantation Embryo Development. ACS Photonics **10**(12), 4177–4187 (2023) https://doi.org/10.1021/acsphotonics.3c00900

[15] Hedde, P.N., Cinco, R., Malacrida, L., Kamaid, A., Gratton, E.: Phasor-based hyperspectral snapshot microscopy allows fast imaging of live, three-dimensional

tissues for biomedical applications. Communications Biology **4**(1), 1–11 (2021) https://doi.org/10.1038/s42003-021-02266-z

[16] Wang, P., Kitano, M., Keomanee-Dizon, K., Truong, T.V., Fraser, S.E., Cutrale, F.: A single-shot hyperspectral phasor camera for fast, multi-color fluorescence microscopy. Cell Reports Methods **3**(4), 100441 (2023) https://doi.org/10.1016/j.crmeth.2023.100441

[17] Dvornikov, A., Gratton, E.: Hyperspectral imaging in highly scattering media by the spectral phasor approach using two filters. Biomedical Optics Express **9**(8), 3503–3511 (2018) https://doi.org/10.1364/BOE.9.003503

[18] Cao, X., Yue, T., Lin, X., Lin, S., Yuan, X., Dai, Q., Carin, L., Brady, D.J.: Computational Snapshot Multispectral Cameras: Toward dynamic capture of the spectral world. IEEE Signal Processing Magazine **33**(5), 95–108 (2016) https://doi.org/10.1109/MSP.2016.2582378

[19] Candes, E.J., Wakin, M.B.: An Introduction To Compressive Sampling. IEEE Signal Processing Magazine **25**(2), 21–30 (2008) https://doi.org/10.1109/MSP.2007.914731

[20] LeCun, Y., Bengio, Y., Hinton, G.: Deep learning. Nature **521**(7553), 436–444 (2015) https://doi.org/10.1038/nature14539

[21] Arridge, S., Maass, P., Öktem, O., Schönlieb, C.-B.: Solving inverse problems using data-driven models. Acta Numerica **28**, 1–174 (2019) https://doi.org/10.1017/S0962492919000059

[22] Barbastathis, G., Ozcan, A., Situ, G.: On the use of deep learning for computational imaging. Optica **6**(8), 921–943 (2019) https://doi.org/10.1364/OPTICA.6.000921

[23] Gedalin, D., Oiknine, Y., Stern, A.: DeepCubeNet: Reconstruction of spectrally compressive sensed hyperspectral images with deep neural networks. Optics Express **27**(24), 35811–35822 (2019) https://doi.org/10.1364/OE.27.035811

[24] Baek, S.-H., Ikoma, H., Jeon, D.S., Li, Y., Heidrich, W., Wetzstein, G., Kim, M.H.: End-to-End Hyperspectral-Depth Imaging with Learned Diffractive Optics. arXiv:2009.00463 [cs, eess] (2020) arXiv:2009.00463 [cs, eess]

[25] Duarte, M.F., Davenport, M.A., Takhar, D., Laska, J.N., Sun, T., Kelly, K.F., Baraniuk, R.G.: Single-Pixel Imaging via Compressive Sampling. Signal Processing Magazine, IEEE **25**(2), 83–91 (2008) https://doi.org/10.1109/MSP.2007.914730

[26] Zhang, Z., Ma, X., Zhong, J.: Single-pixel imaging by means of Fourier spectrum acquisition. Nature Communications **6**(1), 6225 (2015) https://doi.org/10.1038/ncomms7225

[27] Hahamovich, E., Monin, S., Hazan, Y., Rosenthal, A.: Single pixel imaging at megahertz switching rates via cyclic Hadamard masks. Nature Communications **12**(1), 4516 (2021) https://doi.org/10.1038/s41467-021-24850-x

[28] Xu, Y., Lu, L., Saragadam, V., Kelly, K.F.: A compressive hyperspectral video imaging system using a single-pixel detector. Nature Communications **15**(1), 1456 (2024) https://doi.org/10.1038/s41467-024-45856-1

[29] Lorente Mur, A., Leclerc, P., Peyrin, F., Ducros, N.: Single-pixel image reconstruction from experimental data using neural networks. Optics Express **29**(11), 17097–17110 (2021) https://doi.org/10.1364/OE.424228

[30] Power, R.M., Huisken, J.: A guide to light-sheet fluorescence microscopy for multiscale imaging. Nature Methods **14**(4), 360–373 (2017) https://doi.org/10.1038/

nmeth.4224

[31] Crombez, S., Leclerc, P., Ray, C., Ducros, N.: Computational hyperspectral light-sheet microscopy. Optics Express **30**(4), 4856–4866 (2022) https://doi.org/10.1364/OE.442043

[32] Sloane, N.J.A., Harwit, M.: Masks for Hadamard transform optics, and weighing designs. Applied Optics **15**(1), 107–114 (1976) https://doi.org/10.1364/AO.15.000107

[33] Lawson, N.D., Weinstein, B.M.: In vivo imaging of embryonic vascular development using transgenic zebrafish. Developmental Biology **248**(2), 307–318 (2002) https://doi.org/10.1006/dbio.2002.0711

[34] Fontenas, L., Welsh, T.G., Piller, M., Coughenour, P., Gandhi, A.V., Prober, D.A., Kucenas, S.: The Neuromodulator Adenosine Regulates Oligodendrocyte Migration at Motor Exit Point Transition Zones. Cell Reports **27**(1), 115–1285 (2019) https://doi.org/10.1016/j.celrep.2019.03.013

[35] Lambert, T.J.: FPbase: A community-editable fluorescent protein database. Nature Methods **16**(4), 277–278 (2019) https://doi.org/10.1038/s41592-019-0352-8

[36] Kwak, J., Park, O.K., Jung, Y.J., Hwang, B.J., Kwon, S.-H., Kee, Y.: Live Image Profiling of Neural Crest Lineages in Zebrafish Transgenic Lines. Molecules and Cells **35**(3), 255–260 (2013) https://doi.org/10.1007/s10059-013-0001-5

[37] Thorn, K.: Genetically encoded fluorescent tags. Molecular Biology of the Cell **28**(7), 848–857 (2017) https://doi.org/10.1091/mbc.e16-07-0504

[38] Harwit, M., Sloane, N.J.A.: Hadamard Transform Optics. Academic Press, ???

(1979)

[39] Chang, B.-J., Perez Meza, V.D., Stelzer, E.H.K.: csiLSFM combines light-sheet fluorescence microscopy and coherent structured illumination for a lateral resolution below 100 nm. Proceedings of the National Academy of Sciences **114**(19), 4869–4874 (2017) https://doi.org/10.1073/pnas.1609278114

[40] Mazzella, L., Mangeat, T., Giroussens, G., Rogez, B., Li, H., Creff, J., Saadaoui, M., Martins, C., Bouzignac, R., Labouesse, S., Idier, J., Galland, F., Allain, M., Sentenac, A., LeGoff, L.: Extended-depth of field random illumination microscopy, EDF-RIM, provides super-resolved projective imaging. Light: Science & Applications **13**(1), 285 (2024) https://doi.org/10.1038/s41377-024-01612-0

[41] Loncan, L., Almeida, L.B., Bioucas-Dias, J.M., Briottet, X., Chanussot, J., Dobigeon, N., Fabre, S., Liao, W., Licciardi, G.A., Simões, M., Tourneret, J., Veganzones, M.A., Vivone, G., Wei, Q., Yokoya, N.: Hyperspectral Pansharpening: A Review. IEEE Geoscience and Remote Sensing Magazine **3**(3), 27–46 (2015) https://doi.org/10.1109/MGRS.2015.2440094

[42] Calisesi, G., Castriotta, M., Candeo, A., Pistocchi, A., D'Andrea, C., Valentini, G., Valentini, G., Farina, A., Bassi, A., Bassi, A.: Spatially modulated illumination allows for light sheet fluorescence microscopy with an incoherent source and compressive sensing. Biomedical Optics Express **10**(11), 5776–5788 (2019) https://doi.org/10.1364/BOE.10.005776

[43] Zunino, A., Garzella, F., Trianni, A., Saggau, P., Bianchini, P., Diaspro, A., Duocastella, M.: Multiplane Encoded Light-Sheet Microscopy for Enhanced 3D Imaging. ACS Photonics **8**(11), 3385–3393 (2021) https://doi.org/10.1021/acsphotonics.1c01401

[44] Daetwyler, S., Fiolka, R.P.: Light-sheets and smart microscopy, an exciting future is dawning. Communications Biology **6**(1), 1–11 (2023) https://doi.org/10.1038/s42003-023-04857-4

[45] Monga, V., Li, Y., Eldar, Y.C.: Algorithm Unrolling: Interpretable, Efficient Deep Learning for Signal and Image Processing. IEEE Signal Processing Magazine **38**(2), 18–44 (2021) https://doi.org/10.1109/MSP.2020.3016905

[46] Zhang, K., Li, Y., Zuo, W., Zhang, L., Van Gool, L., Timofte, R.: Plug-and-Play Image Restoration With Deep Denoiser Prior. IEEE Transactions on Pattern Analysis and Machine Intelligence **44**(10), 6360–6376 (2022) https://doi.org/10.1109/TPAMI.2021.3088914

[47] Pronina, V., Lorente Mur, A., Abascal, J.F.P.J., Peyrin, F., Dylov, D.V., Ducros, N.: 3D denoised completion network for deep single-pixel reconstruction of hyperspectral images. Optics Express **29**(24), 39559 (2021) https://doi.org/10.1364/OE.443134

[48] Lee, D.D., Seung, H.S.: Learning the parts of objects by non-negative matrix factorization. Nature **401**(6755), 788–791 (1999) https://doi.org/10.1038/44565

[49] Hariga, S., Cohen, J.E., Ducros, N.: Joint Reconstruction and Spectral Unmixing from Single-Pixel Acquisitions. In: 2024 32nd European Signal Processing Conference (EUSIPCO), pp. 661–665. IEEE, Lyon, France (2024). https://doi.org/10.23919/EUSIPCO63174.2024.10715454

[50] Bro, R., De Jong, S.: A fast non-negativity-constrained least squares algorithm. Journal of Chemometrics **11**(5), 393–401 (1997) https://doi.org/10.1002/(SICI)1099-128X(199709/10)11:5<393::AID-CEM483>3.0.CO;2-L

[51] Beneti Martins, G., Mahieu-Williame, L., Baudier, T., Ducros, N.: OpenSpyrit:

An ecosystem for open single-pixel hyperspectral imaging. Optics Express **31**(10), 15599 (2023) https://doi.org/10.1364/OE.483937

[52] Paszke, A., Gross, S., Massa, F., Lerer, A., Bradbury, J., Chanan, G., Killeen, T., Lin, Z., Gimelshein, N., Antiga, L., Desmaison, A., Kopf, A., Yang, E., DeVito, Z., Raison, M., Tejani, A., Chilamkurthy, S., Steiner, B., Fang, L., Bai, J., Chintala, S.: PyTorch: An imperative style, high-performance deep learning library. In: Wallach, H., Larochelle, H., Beygelzimer, A., dAlché-Buc, F., Fox, E., Garnett, R. (eds.) Advances in Neural Information Processing Systems 32, pp. 8024–8035. Curran Associates, Inc., ??? (2019)

[53] Russakovsky, O., Deng, J., Su, H., Krause, J., Satheesh, S., Ma, S., Huang, Z., Karpathy, A., Khosla, A., Bernstein, M., Berg, A.C., Fei-Fei, L.: ImageNet Large Scale Visual Recognition Challenge. International Journal of Computer Vision **115**(3), 211–252 (2015) https://doi.org/10.1007/s11263-015-0816-y